Journal of
Materials Chemistry A

PAPER

View Article Online
View Journal | View Issue

Published on 05 December 2023. Downloaded by University of Rochester on 2/27/2024 7:35:54 PM.

Check for updates

Cite this: *J. Mater. Chem. A*, 2024, **12**, 1517

Potassium supporting electrolyte enhances stability of Ti-substituted polyoxovanadates for nonaqueous redox flow batteries†

Mamta Dagar, William W. Brennessel and Ellen M. Matson *

A bottleneck in the development of efficient and energy-dense electrochemical energy storage systems is limited strategies to enhance the stability of the charge carriers. While molecular engineering can allow desirable electrochemical properties of the active material to be achieved, understanding intermolecular interactions among species within the electrolyte can yield robust systems for practical applications. Here, we discuss the role of counter cations of the supporting electrolyte on the electrochemical stability and battery performance of the di-titanium substituted polyoxovanadate–alkoxide cluster, $[Ti_2V_4O_5(OMe)_{14}]$. Our results illustrate unique cation pairing effects associated with the use of alkali salts, MPF_6 ($M = Li^+, K^+$), with the potassium-derived supporting electrolyte resulting in enhanced stability of reduced forms of the cluster. Single-crystal X-ray diffraction studies indicate that the cluster cores are linked by potassium atoms as contact ion-pairs. The results provide insight into the role of supporting electrolyte on the (electro)chemical stability of polyoxovanadate charge carriers.

Received 22nd October 2023
Accepted 4th December 2023

DOI: 10.1039/d3ta06432h

rsc.li/materials-a

Introduction

Redox flow batteries (RFBs) are stationary electrochemical energy storage devices that store energy in the form of charged, soluble, redox-active molecules in solution.[1,2] They are a promising solution for grid-scale energy storage due to their high scalability and characteristic decoupled energy and power.[3] Decoupled energy and power refers to the ability to control energy storage and power output independently by separately scaling the electrolyte storage tanks and electrode surface area. RFBs can be classified as aqueous or non-aqueous, depending upon the supporting electrolyte composition. Compared with aqueous RFBs, non-aqueous RFBs (NAqRFBs) offer a wide range of working temperatures and high cell voltages due to the greater stability of organic solvents over a large potential range.[4] However, the implementation of this technology in grid-scale energy storage remains limited by high costs and low energy densities as compared to Li-ion batteries.[5]

A non-aqueous battery electrolyte consists of three primary components – active material, solvent, and supporting electrolyte. Justification for the investigation of alternative supporting electrolytes, and their interactions with established redox mediators, is derived from technoeconomic models which quote the capital costs of redox-active molecules and supporting electrolytes as proportional to their equivalent weights.[6,7] The US Department of Energy Office of Electricity has targeted the optimal cost for future RFBs as \$150 kW^{-1} h^{-1}.[8] While it can be difficult to modulate the cost of a charge carrier owing to their desirable physicochemical properties, it is feasible to meet the cost stipulations by identifying lighter supporting electrolytes.

Tetraalkylammonium salts are ubiquitous in NAqRFB literature due to their limited interactions with charged forms of molecules, which often enables reversible redox chemistry. However, their bulky nature increases the equivalent weight of the redox system that hampers the ability to achieve high gravimetric energy densities. This drawback makes small alkali ions an attractive choice as alternative supporting electrolytes. Additionally, cations with coordinating properties can aid in tuning the stability of the ionic species in the electrolyte through charge compensation.[9,10] While the development of suitable charge carriers can yield electrolytes with improved properties such as high ionic conductivity and stability, these properties can be further modulated through the intermolecular interactions between the species present within the electrolyte system. Several studies have utilized these favorable ion-pairing interactions to improve the redox potentials of cathode materials.[11,12] However, the gamut of work is concentrated in the domain of carbonyl-based organic charge carriers in NAqRFB literature and fewer reports have explored this avenue for metal-based charge carriers.[13–15] Mitchell and Elgrishi have demonstrated that iron(III) tetraphenylporphyrin chloride is incompatible with tetraalkylammonium salts as Fe(0) formed during battery cycling reacts with these cations. The authors suggest that to implement iron tetraphenylporphyrins as

---

Department of Chemistry, University of Rochester, Rochester, NY 14627, USA. E-mail: matson@chem.rochester.edu

† Electronic supplementary information (ESI) available. CCDC 2302646. For ESI and crystallographic data in CIF or other electronic format see DOI: **https://doi.org/10.1039/d3ta06432h**

Published on 05 December 2023. Downloaded by University of Rochester on 2/27/2024 7:35:54 PM.

possible candidates for redox flow battery systems, tetrabutylammonium hexafluorophosphate ($TBAPF_6$) needs to be substituted by potassium salts to inhibit side reactivity of the electrolyte.[16] Thus, despite the profound impact that the spectator ions of the supporting salt can have on the stability of the electrolyte system, this is an often-overlooked aspect in the development of NAqRFB technology.

Inorganic cluster complexes are promising candidates as charge carriers for NAqRFB applications because they exhibit high stability across multiple oxidation states that provides wide range of redox potentials.[17–21] Over the past decade, our group has established polyoxovanadate–alkoxide (POV–alkoxide) clusters as a unique class of charge carriers for deployment in symmetric NAqRFBs (Fig. 1).[22–25] We have demonstrated the efficacy of these inorganic assemblies in electrochemical energy storage (EES) by probing the structure–function relationships that manifest in optimized physicochemical properties and can be used to guide the design of active materials. Heterometal installation in the POV framework serves to widen the operable potential window while retaining the characteristic electrochemical reversibility and stability of the homometallic POV–alkoxide.[26,27] These properties render the heterometallic Lindqvist clusters as better charge carriers for applications in NAqRFBs than their homometallic congeners – the wide potential window increases the attainable energy density of the system. Unfortunately, transition metal-doped POV–alkoxide clusters are plagued by reductive instability during long-term charge/discharge cycling experiments. The identification of (electro)chemical routes to enhance the stability of these active materials across all charged states is key for the rational design of functional batteries invoking heterometallic POV–alkoxide clusters as charge carriers.

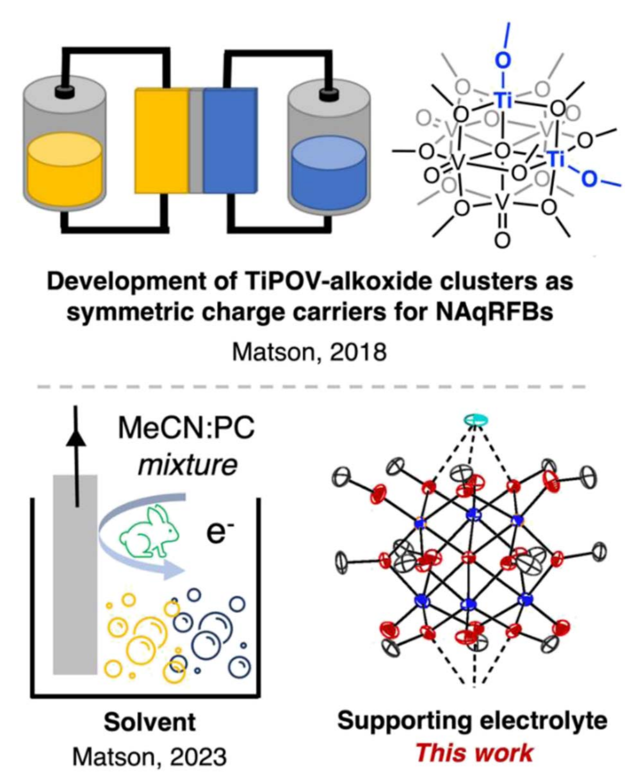

Fig. 1 Summary of our research team's progress in tuning the composition of the electrolyte system for improved NAqRFBs.

The intermolecular interactions between alkali ions and redox active materials can be used to regulate the electrochemical properties in RFBs without changing the molecular structure of the charge carrier.[28,29] Previously, our group has demonstrated that the all vanadium homometallic POV–alkoxide cluster, $[V_6O_7(OCH_3)_{12}]$, acts as a homogeneous model of pseudocapacitive electrodes due to differing range of ion-pairing interactions with alkali cations.[30] Specifically, we observed that the reduction processes in the homometallic system are sensitive to the identity of the compensating cation, exhibiting the full continuum between nonspecific and specific binding interactions in the series from alkyl ammonium to lithium ions. Motivated by these results, we became interested in evaluating the effect of supporting electrolyte on the well-established titanium-substituted POV–alkoxide charge carrier, $[Ti_2V_4O_5(OMe)_{14}]$, by our team.[27,31] We hypothesized that ionic binding between an alkali ion and the monoanionic, reduced form of the POV–alkoxide cluster would improve the stability of the assembly during cycling experiments.

Herein, we report the role of supporting electrolyte on the stability of the reduced form of the titanium-substituted POV–alkoxide clusters. We evaluate the compatibility of alkali metal electrolytes by utilizing MPF_6 ($M = Li, K$) supporting salts, comparing their cyclic voltammograms under identical experimental conditions. While an ideal supporting electrolyte should be inert, specific non-covalent interactions between the redox inactive ions, solvent molecules, and the active species can result in improved stability in otherwise unstable charged states. Cyclic voltammetry experiments demonstrate such interactions are operative in the case of $[Ti_2V_4O_5(OMe)_{14}]$; the heterometallic POV–alkoxide cluster exhibits degradation in Li-based electrolytes. However, the use of potassium hexafluorophosphate (KPF_6) not only enhances the stability of the reduced cluster, but also improves capacity and minimizes degradation of the active material during battery cycling. These results demonstrate the critical role that the supporting electrolyte can play in NAqRFBs and provide a new rationale for selecting the appropriate counter ions in screening charge carriers.

Experimental

General considerations

All manipulations were carried out in the absence of water and oxygen in a UniLab MBraun inert atmosphere glovebox under a dinitrogen atmosphere. Glassware was oven dried for a minimum of 4 hours and cooled in an evacuated antechamber prior to use. Acetonitrile (MeCN) and dimethylformamide (DMF) were dried and deoxygenated on a Glass Contour System (Pure Process Technology, LLC) and stored over activated 3 Å molecular sieves purchased from Fisher Scientific. Lithium hexafluorophosphate ($LiPF_6$), potassium hexafluorophosphate

Published on 05 December 2023. Downloaded by University of Rochester on 2/27/2024 7:35:54 PM.

(KPF_6), lithium triflouromethanesulfonate (LiOTf), and tetrabutylammonium hexafluorophosphate ($TBAPF_6$) were purchased from Sigma-Aldrich. $TBAPF_6$ was recrystallized thrice using hot methanol and stored under dynamic vacuum for a minimum of two days prior to use. $LiPF_6$, KPF_6, and LiOTf were dried over P_2O_5 for at least 24 h before use. $[Ti_2V_4O_5(OMe)_{14}]$ was synthesized according to literature precedent.[32]

^1H NMR spectra were recorded at 500 MHz on Bruker DPX-500 spectrometer locked on the signal of deuterated solvents. All chemical shifts were reported relative to the peak of residual ^1H signal in deuterated solvents.[33] Deuterated acetonitrile (CD_3CN) was purchased from Cambridge Isotope Laboratories and used as received. Electronic absorption measurements were recorded at room temperature in acetonitrile (MeCN) in a sealed 1 cm quartz cuvette with an Agilent Cary 60 UV/Vis spectrophotometer. Infrared spectra were recorded on a Shimadzu IRAffinity-1 Fourier Transform Infrared spectrophotometer and are reported in wavenumbers (cm^{-1}). Elemental analysis was performed by Midwest Microlabs (Indianapolis, Indiana). X-ray quality single crystals were mounted on a thin Nylon loop and positioned on a XtaLab Synergy-S Dualflex diffractometer equipped with a HyPix-6000He HPC area detector for data collection at 100.0(5) K. Structure solutions were obtained using SHELXT-2014/5 and refined using SHELXL-2014/7.[34]

Cyclic voltammetry

Cyclic voltammetry (CV) was performed using a three-electrode setup inside a nitrogen filled glove box (MBraun UniLab, USA) using a Bio-Logic SP 150 potentiostat/galvanostat and the EC-Lab software suite. The concentration of $[Ti_2V_4O_5(OMe)_{14}]$ and the supporting electrolytes ($LiPF_6$, KPF_6, $TBAPF_6$, LiOTf) were kept at 5 mM and 100 mM, respectively, throughout all measurements. CVs were recorded using a 3 mm diameter glassy carbon working electrode (CH Instruments, USA), a Pt wire auxiliary electrode (CH Instruments, USA), and an Ag/Ag^+ non-aqueous reference electrode with 0.01 M $AgNO_3$ in 0.1 M $TBAPF_6$ in acetonitrile (BASi, USA). CVs were *iR* compensated at 95% with impedance taken at 100 kHz using the ZIR tool included within the EC-Lab software. The remaining 5% uncompensated resistance was accounted for by manual correction.[35]

Square wave voltammetry

Square wave voltammetry (SWV) was performed using a three-electrode setup inside a nitrogen filled glove box (MBraun UniLab, USA) using a Bio-Logic SP 150 potentiostat/galvanostat and the EC-Lab software suite. All experiments were carried out at room temperature inside a nitrogen-filled glove box (MBraun, USA). All SWV measurements were *iR* compensated at 85% with impedance taken at 100 kHz using the ZIR tool included with the EC-Lab software. Square wave experiments were conducted at 50 mV s^{-1} (pulse height: 25 mV, pulse width: 100 ms, step height: 10 mV).

Bulk electrolysis

Bulk electrolysis experiments were performed in a H-cell with a glass frit separator (porosity = 10–16 μm, Pine Research, USA) using a Bio-Logic SP 150 potentiostat/galvanostat. In all experiments, an active species concentration of 5 mM was used. The working electrode compartment contained 5 mL of the active species with 0.1 M supporting electrolyte $TBAPF_6$ or KPF_6) in the desired solvent (acetonitrile or dimethylformamide), while the counter electrode compartment had 5 mL of 0.1 M supporting electrolyte in the same solvent (acetonitrile or dimethylformamide). A Pt mesh working electrode and a Pt wire counter electrode were used. Bulk electrolysis experiments were carried out using the chronoamperometry techniques available in EC-Lab software suite at constant potentials, selected from CV.

Solubility measurements

A 0.1 M concentration of KPF_6 was used in all samples to simulate electrochemical conditions and all samples were referenced against a baseline of 0.1 M KPF_6 in acetonitrile. To establish a calibration curve, 10 mM stock solutions were prepared by combining 100 mM of the supporting electrolyte (0.092 g KPF_6), 0.041 g $[Ti_4V_4O_5(OMe)_{14}]$ of and 5 mL of solvent in a vial and stirring until completely dissolved. Additionally, a stock solution of 0.1 M KPF_6 was prepared by combining 0.276 g KPF_6, in 15 mL of acetonitrile. In a cuvette, 0.3 mL of the cluster stock solution was added and was subsequently diluted with 2.7 mL of the 0.1 M KPF_6 stock solution. This process was repeated 4 times to obtain solutions with the following concentrations: 1.0 mM, 0.8 mM, 0.6 mM, 0.4 mM, and 0.2 mM. The electronic absorption spectra (UV-Vis) of these samples were recorded, and their absorbances at 420 nm were plotted against the sample's concentration to obtain a Beer's law equation.

Three saturated solutions for each solvent were prepared by stirring an excess of Ti-POV in 5 mL of 0.1 M electrolyte (KPF_6) solution for a minimum of 24 hours. These solutions were passed through a syringe filter (EZFlow Syringe Filter, diameter = 25 mm, pore size = 0.22 μm) to remove undissolved Ti-POV. 20 μL aliquots of each solution were removed and diluted such that the absorbance of the sample fell between 0.1 and 1.0. The absorbance of each diluted sample at 420 nm was recorded, and the concentration of the diluted sample was determined using the Beer's law equation from the corresponding calibration curve. The concentration of each saturated solution was then calculated from the concentration of the diluted sample. See ESI† for figures and details pertaining to the solubility calculations performed for the Ti-substituted POV–alkoxide cluster reported.

Charge/discharge experiments

Charge–discharge cycling experiments were conducted in a nitrogen filled glove box using a glass H-cell separated by a microporous glass frit (P5, 1.6 μm, Adams and Chittenden, USA) and a Bio-Logic SP 300 potentiostat/galvanostat. The electrolyte solutions used in charge–discharge experiments were 5 mM Ti-POV in 0.1 M electrolyte ($TBAPF_6$ or KPF_6) in acetonitrile. Each compartment of the H-cell was filled with 5.0 mL of electrolyte solution. Two graphite felt electrodes (1 × 1 × 0.5 cm, Fuel Cell Store, USA) were placed in the posolyte and

Published on 05 December 2023. Downloaded by University of Rochester on 2/27/2024 7:35:54 PM.

negolyte chambers. Electrodes were attached to Pt wire current collectors submerged in the electrolyte solutions (~0.5 cm). Graphite felt electrodes were soaked in electrolyte solutions for 24 hours before each experiment. A sequential galvanostatic–potentiostatic charge–discharge method was adopted using a charging current of 0.2 mA until the potential reached 1.9 V.[36] Subsequently, the potential was held at 1.9 V until the current dropped to 0.02 mA. Similarly, a discharging current of 0.2 mA was applied until a cut-off potential of 1.4 V was reached, followed by a potentiostatic discharge at 1.4 V until the current reached a value of 0.02 mA. For the duration of the charge–discharge experiments, both half cells were stirred at ~1000 rpm.

Synthesis of $[K\{Ti_2V_4O_5(OCH_3)_{14}\}]$

In a nitrogen filled glovebox (MBraun UniLab, USA), $[Ti_2V_4O_5(OMe)_{14}]$ (0.02 g, 0.025 mmol) was taken in a 20 mL scintillation vial and dissolved in 10 mL THF. To this solution, KC_8 (0.01 g, 0.075 mmol) was weighed by difference and the contents were allowed to stir for 3 h. The black mixture was passed over Celite using a pipette filter to remove residual graphite and the filtrate was evaporated under vacuum. The obtained reddish-brown powder was washed with pentane (10 mL) and diethyl ether (10 mL). Volatiles were removed under pressure to give a dark orange product. Yield: 0.02 g, 0.024 mmol, 97%. Crystals suitable for X-ray analysis were obtained using slow evaporation of a concentrated solution of the TiPOV in acetonitrile. ^1H NMR (500 MHz, CD_3CN) $\delta = -12.96, -6.98, 1.84, 10.35, 12.65, 13.74, 24.97$ ppm. FT-IR (ATR, cm^{-1}): 1127 (O_t-CH_3), 1034 (O_b-CH_3), 978 (V═O). UV-Vis (CH_3CN, 21 °C) λ = 430 nm (ε = 222 M^{-1} cm^{-1}), 625 nm (ε = 70 M^{-1} cm^{-1}). Elemental analysis for $C_{14}H_{42}KO_{19}Ti_2V_4\cdot 3/5CH_3CN$ (M_w = 877.7 g mol^{-1}): calc. C, 20.8; H, 5.03; N, 0.96. Found, C, 20.827; H, 4.705; N: 0.992.

Results and discussion

The cyclic voltammogram (CV) of the heterometallic cluster $[Ti_2V_4O_5(OMe)_{14}]$ collected in MeCN with $TBAPF_6$ as the supporting electrolyte reveals four quasi-reversible, one-electron redox events located at $E_{1/2}$ values of −2.10 V, −1.58 V, +0.15 V, +0.64 V (*vs.* Ag^+/Ag, Scheme 1 and Fig. 2).[27] The two reduction events ($E_{1/2}$ = −1.58 V, R1; −2.10 V, R2) are assigned to the sequential reductions of the two titanium ions embedded within the Lindqvist core ($Ti^{IV} \rightarrow Ti^{III}$), whereas the two oxidation events ($E_{1/2}$ = +0.15 V, O1; +0.64 V, O2) are associated with the sequential oxidation of two vanadium centers ($V^{IV} \rightarrow V^{V}$).[27] With this understanding of the electrochemistry of the TiPOV in the presence of non-coordinating TBA ions, we turned our attention to the investigation of the effect of alkali salts on the electrochemical profile of the organofunctionalized hexametalate assembly.

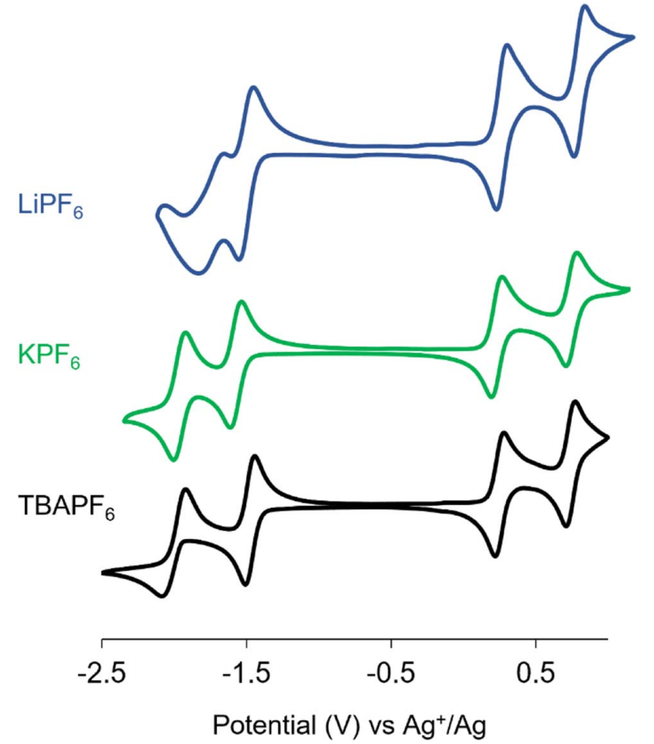

Fig. 2 Cyclic voltammograms of 5 mM solutions of $[Ti_2V_4O_5(OMe)_{14}]$ in acetonitrile with 0.1 M supporting electrolyte (blue = $LiPF_6$, green = KPF_6, black = $TBAPF_6$) recorded at a scan rate of 20 mV s^{-1}.

We recorded CVs of $[Ti_2V_4O_5(OMe)_{14}]$ in MeCN using 0.1 M $LiPF_6$ and KPF_6 as the supporting electrolyte. As depicted in Fig. 2, the voltametric response of $[Ti_2V_4O_5(OMe)_{14}]$ varies as the supporting electrolyte is changed. We note that there are no obvious variations in the oxidation events of the cluster in the presence of alkali ions, consistent with our expectation that the positively charged clusters formed following oxidation will not interact extensively with the alkali metals in the solution. However, significant changes in the reductive region

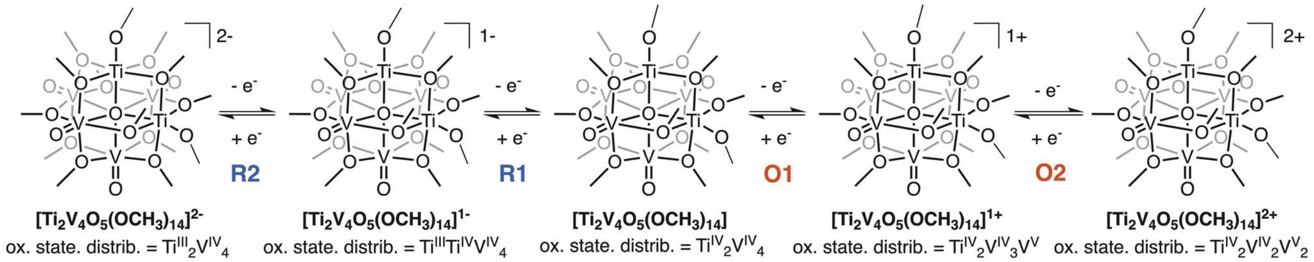

Scheme 1 Redox chemistry of $[Ti_2V_4O_5(OCH_3)_{14}]$.

This journal is © The Royal Society of Chemistry 2024

Published on 05 December 2023. Downloaded by University of Rochester on 2/27/2024 7:35:54 PM.

of the voltammogram of $[Ti_2V_4O_5(OMe)_{14}]$ are observed in the presence of alkali salts. The two negative redox events in the CV of the cluster ($E_{1/2} = -1.58$ V, -2.10 V) in $TBAPF_6$ shift towards positive potentials in the presence of alkali cations. The magnitude of these shifts increases ($LiPF_6$: $E_{1/2} = -1.44$ V, -1.62 V and KPF_6: $E_{1/2} = -1.57$ V, -1.94 V) as the size of the alkali metal decreases. The difference is more pronounced for the most reducing redox wave (R2), whose reduction potential is positively shifted by 480 mV in $LiPF_6$ as compared to 160 mV in the presence of KPF_6 (all voltages reported *vs.* $E_{1/2}$ values obtained with $TBAPF_6$ as the supporting electrolyte). We hypothesize that this is due to the electrostatic interactions between the anionic forms of the cluster in its reduced state(s) and the alkali metal cations. This supposition frames our subsequent investigations, focused on interrogating the influence of alkali ions on the stability of the reduced form of $[Ti_2V_4O_5(OCH_3)_{14}]$, and thus the overall performance and durability of the battery.

Effect of supporting cations on the reductive stability of $[Ti_2V_4O_5(OMe)_{14}]$

As described above, the voltametric response observed *via* CV suggests ion-pairing interactions are present between the alkali metal cations and the reduced forms of the cluster. This effect seems more prominent in the presence of Li^+ ions as compared to K^+. To refine the consequences on reduction events as a function of ion pairing interactions, we performed square wave voltammetry (SWV) in the presence of increasing concentrations of MPF_6 (M = Li, K; Fig. 3). The motivation behind these experiments stems from our prior work where SWV measurements aided in clearly describing the charge compensation phenomena in the presence of alkali ions.[30] We began our investigations by analyzing the electrochemical response generated by substoichiometric additions of $LiPF_6$ to the cluster solution (Fig. 3a and Table S1†). We observe that the intensities of peaks observed in the SWV waves associated with the reduction events decrease monotonically as $LiPF_6$ is added due to the dilution of the cluster solution upon successive additions of the titrant (Fig. 3a). Furthermore, there is a gradual shift in the potentials of the Ti-based reductions upon addition of subsequent equivalents of $LiPF_6$. This shift towards positive voltages is more prominent for R2 (-2.10 V to -1.98 V) as compared to R1 at -1.59 V. Notably, following addition of two equivalents of $LiPF_6$, complete loss of the electrochemical feature originally at -2.10 V is observed. The corresponding CVs (Fig. 3c) further highlight this observation. This behavior is a hallmark of an irreversible system, where total absence of

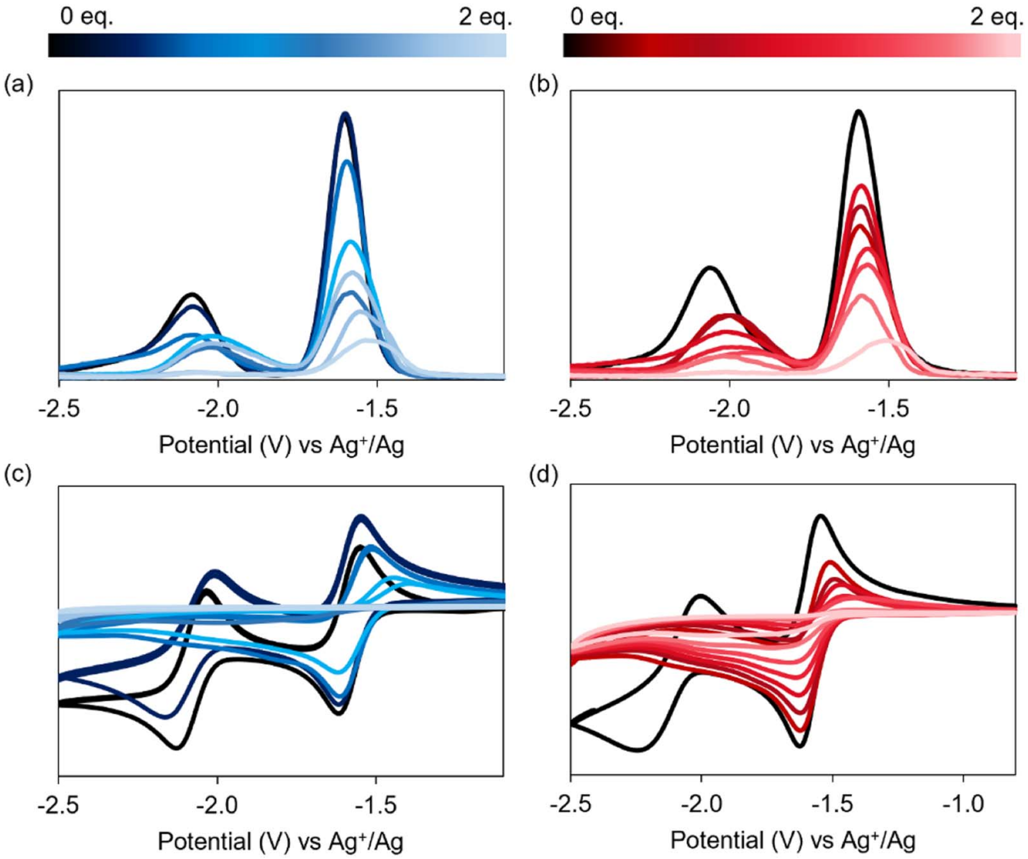

Fig. 3 Square wave voltammograms of titration experiments conducted with substochiometric amounts of (a) $LiPF_6$ (blue) and (b) LiOTf (red) in acetonitrile. All experiments were conducted with initial concentrations of 5 mM $[Ti_2V_4O_5(OMe)_{14}]$ and 0.1 M $TBAPF_6$ as the supporting electrolyte. Equivalents of LiX (X = PF_6 and OTf) were added with respect to $[Ti_2V_4O_5(OMe)_{14}]$. (c and d) Represent the corresponding CVs recorded in each supporting electrolyte.

Published on 05 December 2023. Downloaded by University of Rochester on 2/27/2024 7:35:54 PM.

a reverse peak is observed.[37] One way to resolve these peaks is to record voltammograms at slow scan rates to allow the system to reach a steady state. Thus, we ran CVs of the reduction events at 20 mV s^{-1} and 5 mV s^{-1} (Fig. S1†); however, we did not see significant changes in the electrochemical profile of the voltammograms.

It should be noted that $LiPF_6$ has been reported to disproportionate in acetonitrile, generating LiF and PF_5.[38,39] PF_5 is capable of reacting with traces of water in the solvent to generate HF, which would likely degrade the basic vanadium oxide assembly. Thus, to further confirm that the observed electrochemical response is a trademark of the cation alone and not a product of destabilization due to $LiPF_6$, we repeated titration experiments with LiOTf as another supporting electrolyte to attest our results. The SWV of the corresponding titrations with 10 mM LiOTf solution in acetonitrile are presented in Fig. 3b and Table S2.† We see a similar electrochemical response in both Li salts, with complete loss of the most reducing event upon addition of 2 equivalents of LiX ($X = PF_6$, OTf).

After studying the effect of Li^+ ions on the TiPOV–alkoxide cluster, we shifted our focus on elucidating the impact of K^+ on the electrochemical behavior of the heterometallic assembly. Analogous titration experiments with increasing amounts of KPF_6 were performed. As demonstrated in Fig. 4 (Table S3†), there is a shift in the reduction potential of R2 towards positive voltages, whereas R1 has no obvious alteration upon addition of subsequent equivalents of KPF_6. Notably, the most reducing event (R2) shifts in the positive direction by 160 mV ($E_{1/2} = -1.94$ V) in the presence of 0.2 equivalents of KPF_6 and retains this voltage even after the addition of up to 2 equivalents of the supporting salt. Significant changes in the current response during SWV measurements upon successive additions of KPF_6 after introduction of 0.2 equivalents are not observed. Collectively, these observations made during the titration experiments suggest improved reversibility of reduction events of $[Ti_2V_4O_5(OCH_3)_{14}]$ in the presence of KPF_6.

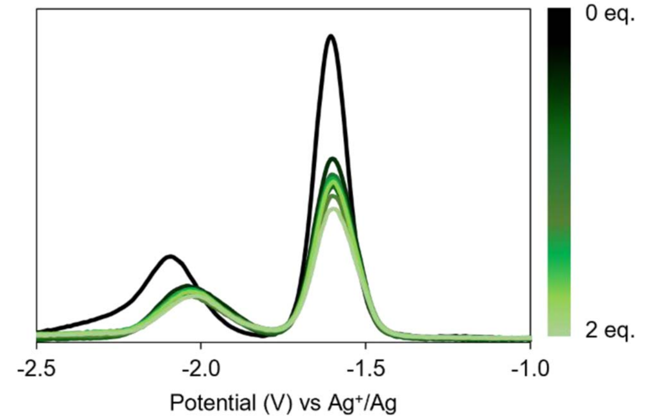

Fig. 4 Electrochemical analysis of titration experiments conducted with substoichiometric amounts of KPF_6. The experiment was conducted with initial concentration of 5 mM $[Ti_2V_4O_5(OMe)_{14}]$ with 0.1 M $TBAPF_6$ in MeCN. Equivalents of KPF_6 were added with respect to $[Ti_2V_4O_5(OMe)_{14}]$.

The differential electrochemical characteristics of the reduction processes of $[Ti_2V_4O_5(OCH_3)_{14}]$ in the presence of disparate alkali ions suggest unique interactions. Hard–soft acid–base (HSAB) theory is often invoked to explain differences in ion-pairing interactions as a function of "hardness". To interrogate the possibility of alkali ions binding to the surface of the TiPOV–alkoxide clusters in solution, titration experiments of the pre-treated solutions of MPF_6 (M = Li, K) with varying volumes of dimethyl formamide (DMF) were performed. DMF was selected for these experiments owing to its high Lewis basic character; indeed this solvent has been reported to have high association constants with alkali ions.[40] We hypothesized that DMF would inhibit the interactions of the alkali salts with the comparatively non-basic surface of the TiPOV–alkoxide cluster. As such, we monitored the amount of DMF required for the regeneration of the voltametric response as observed of the initial CV solution consisting of the TiPOV (recorded in $TBAPF_6$). Fig. 5 represents the corresponding DMF titrations performed on the TiPOV that were pretreated with $LiPF_6$ and KPF_6, respectively. The results demonstrate that the redox events associated with the reduction events shift toward negative potentials upon successive additions of DMF. While addition of 4 mL of DMF in KPF_6 solution yields $E_{1/2}$ values that resemble to those observed for the cluster with 0.1 M $TBAPF_6$ in acetonitrile (Table S4†), it takes only 0.5 mL of DMF in $LiPF_6$ to regenerate these values. The results indicate that all interactions between alkali metal and reduced forms of the cluster have been disrupted by the co-solvent.

The formal potential ($E_{1/2}$) of a redox couple is an indicator of the chemical thermodynamics of the system. We observe that the introduction of alkali metal salts shifts the $E_{1/2}$ values of R2 and R1 towards positive potentials, indicating ion-pairing interactions. As such, the magnitude of change in reduction potentials is attributable to the thermodynamics of ion pairing. Our results indicate that Li^+ has a stronger interaction with the cluster surface than K^+. At first glance, these results are in correspondence with those observed for the all-vanadium system, $[V_6O_7(OCH_3)_{12}]$.[30] In both cases, CV analysis demonstrates stronger charge compensation with Li-based salts. However, subsequent titration experiments performed with DMF give a better insight into the nature of these interactions. While we have proved that Li binds specifically to the hexavanadate surface, the interactions with the Ti substituted POV–alkoxide cluster are much weaker. This is illustrated by the small amount of DMF (0.5 mL) required to disrupt the interactions between Li and the TiPOV. This is likely because the equilibrium favors Li–DMF adduct formation over Li–TiPOV (HSAB principle). In contrast, more volume of DMF (4 mL) is required to disrupt the comparatively weaker interactions of K^+ with the cluster surface. This result is incongruous with that observed for $[V_6O_7(OCH_3)_{12}]$, where K^+ ions exhibit non-specific binding to the cluster core. We ascribe these distinct differences in the types of interactions to the change in basicity of the cluster surface as a result of Ti doping in the hexavanadate system. Introduction of Ti atoms reduces the basicity of the cluster surface. In this regard, the interactions of K^+ with $[Ti_2V_4O_5(OMe)_{14}]^-$ are strong enough to generate a "Goldilocks" scenario that uniquely stabilizes the ensemble.

This journal is © The Royal Society of Chemistry 2024

Published on 05 December 2023. Downloaded by University of Rochester on 2/27/2024 7:35:54 PM.

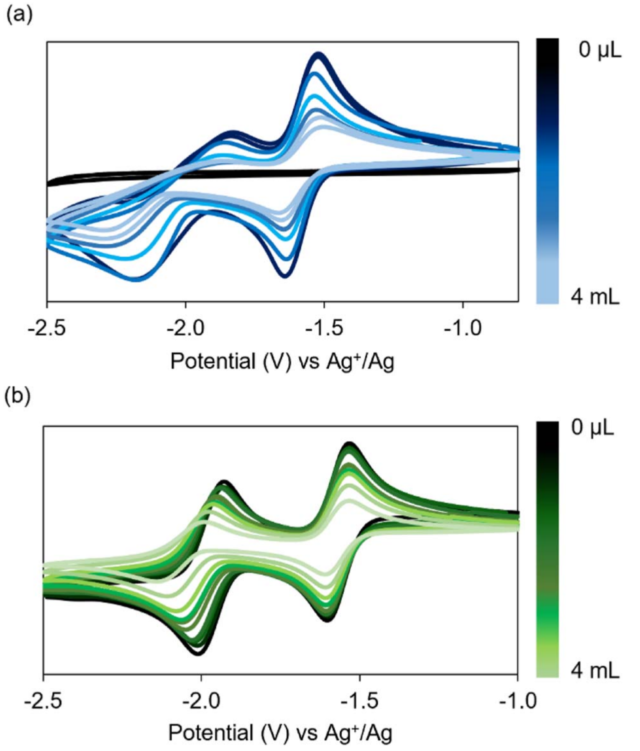

Fig. 5 DMF titrations of the resultant solutions from substoichiometric titrations with (a) $LiPF_6$ (b) KPF_6.

Intrigued by the varied electrochemical response of the cluster in the presence of coordinating cations, we carried out chronoamperometry measurements of the solutions of $[Ti_2V_4O_5(OCH_3)_{14}]$ in MeCN with MPF_6 (M = Li, K) as the supporting electrolyte to assess cluster stability in its reduced and oxidized forms in the presence of alkali salt. Bulk electrolysis of the cluster was performed at potentials selected from the corresponding CVs in the desired supporting electrolyte. Our results demonstrate oxidative stability of the cluster post chronoamperometry in both supporting electrolytes (Fig. S3†). We were especially interested in evaluating the long-term stability of the one electron reduced cluster as a function of the counter cation. Thus, bulk reduction of the TiPOV was performed in 0.1 M MPF_6 (M = Li, K) and the resulting solutions were monitored over a course of one week. Given the closer proximity of R1 and R2 redox events in $LiPF_6$ than KPF_6, we carried out the respective chronoamperometry experiments at −1.6 V and −1.7 V. Post bulk electrolysis, the OCV of the resultant solution shifted from −0.01 V to −1.49 V in $LiPF_6$ and −0.02 V to −1.60 V in KPF_6. These shifts in the reduction potentials demonstrate successful conversion of the neutral species to the mono-reduced cluster (R1). Our results indicate the stability of $[Ti_2V_4O_5(OMe)_{14}]$ in KPF_6, however, decomposition is observed for the Li-based supporting electrolyte (Fig. 6). Long-term stability of the charge carrier is imperative for successful battery cycling. Thus, the instability of the TiPOV–alkoxide assembly in $LiPF_6$ renders it incompatible for charge–discharge experiments.

The improved durability of the heterometallic assembly in the presence of KPF_6 in its reduced form motivates further investigations into structural considerations that promote cluster stability. To this end, we explored the stoichiometric reactivity of the neutral cluster with KC_8 in an attempt to generate the potassium salt of the reduced TiPOV–alkoxide. An excess of reductant was added to $[Ti_2V_4O_5(OCH_3)_{14}]$ in tetrahydrofuran (THF). The reaction mixture was stirred for 3 hours, after which the contents were filtered over Celite to remove the byproduct of the reaction, graphite (Scheme 2, see Experimental section for more details). The product, soluble in MeCN, was initially characterized using CV; four reversible redox events were observed, analogous to the voltammogram reported for $[Ti_2V_4O_5(OCH_3)_{14}]$ (Fig. S4†). However, the open circuit voltage is shifted to −1.62 V, consistent with the formation of the monoreduced cluster. Subsequent characterization of the product *via* ^1H NMR spectroscopy reveals three paramagnetically broadened and shifted signals, ranging from −12.96 to 25.01 ppm (Fig. S5†). The general pattern of these resonances resemble the spectrum reported for $[Ti_2V_4O_5(OCH_3)_{14}]$, however the signals are shifted suggesting a change in the oxidation state of the cluster.[32]

Analysis of the electronic absorption spectrum of $[K\{Ti_2V_4O_5(OCH_3)_{14}\}]$ reveals a broad feature around 430 nm, assigned as an electron transfer event between $V^{IV}(d^1)$ and $Ti^{IV}(d^0)$ ion within the heterometallic clusters.[22] Notably, the molar absorptivity of this absorbance in $[K\{Ti_2V_4O_5(OCH_3)_{14}\}]$ is decreased from that of neutral cluster (from $\varepsilon = 643\ M^{-1}\ cm^{-1}$ to $\varepsilon = 222\ M^{-1}\ cm^{-1}$). The absorption spectrum of the bulk reduced sample in $TBAPF_6$ previously reported by group resembles similar decrease in the molar absorptivity of the transition at 430 nm, albeit to a lesser extent ($\varepsilon = 367\ M^{-1}\ cm^{-1}$).[27] The canonical intervalence charge transfer (IVCT) band characteristic of electron transfer between $V^{IV}(d^1)$ centers and $V^V(d^0)$ centers is absent suggesting that the cluster possess an isovalent V^{IV} electron configuration (Fig. S7†). This is analogous to the observations made for the neutral, homoleptic cluster $[Ti_2V_4O_5(OMe)_{14}]$.[32] This oxidation state distribution is further confirmed by the presence of a weak shoulder around 625 nm, a feature observed in both and the di-anionic hexavanadium cluster, $[V^{IV}{}_6O_7(OCH_3)_{12}]^{2-}$.[41] We note that the electronic absorption spectrum of $[K\{Ti_2V_4O_5(OCH_3)_{14}\}]$ is identical to that observed for the bulk reduced sample in KPF_6 (Fig. S18†). These results further illustrate the ion-pairing interactions between the mono-reduced cluster and K^+ ions formed in solution.

Confirmation of the formation of the potassium salt of the reduced TiPOV–alkoxide cluster was obtained through single crystal X-ray diffraction (Fig. 7, Tables 1 and S5†). Crystals of $[K\{Ti_2V_4O_5(OCH_3)_{14}\}]$ suitable for analysis were grown from slow evaporation of a concentrated solution of the reduced TiPOV–alkoxide cluster in acetonitrile. Refinement of structural data revealed a polymeric structure in one dimension, in which TiPOV–alkoxide clusters are linked by potassium cations as contact ion-pairs. To elucidate the structural consequences of potassium coordination to the surface of the Lindqvist cluster, we compared the bond metrics of $[K\{Ti_2V_4O_5(OCH_3)_{14}\}]$ with

Published on 05 December 2023. Downloaded by University of Rochester on 2/27/2024 7:35:54 PM.

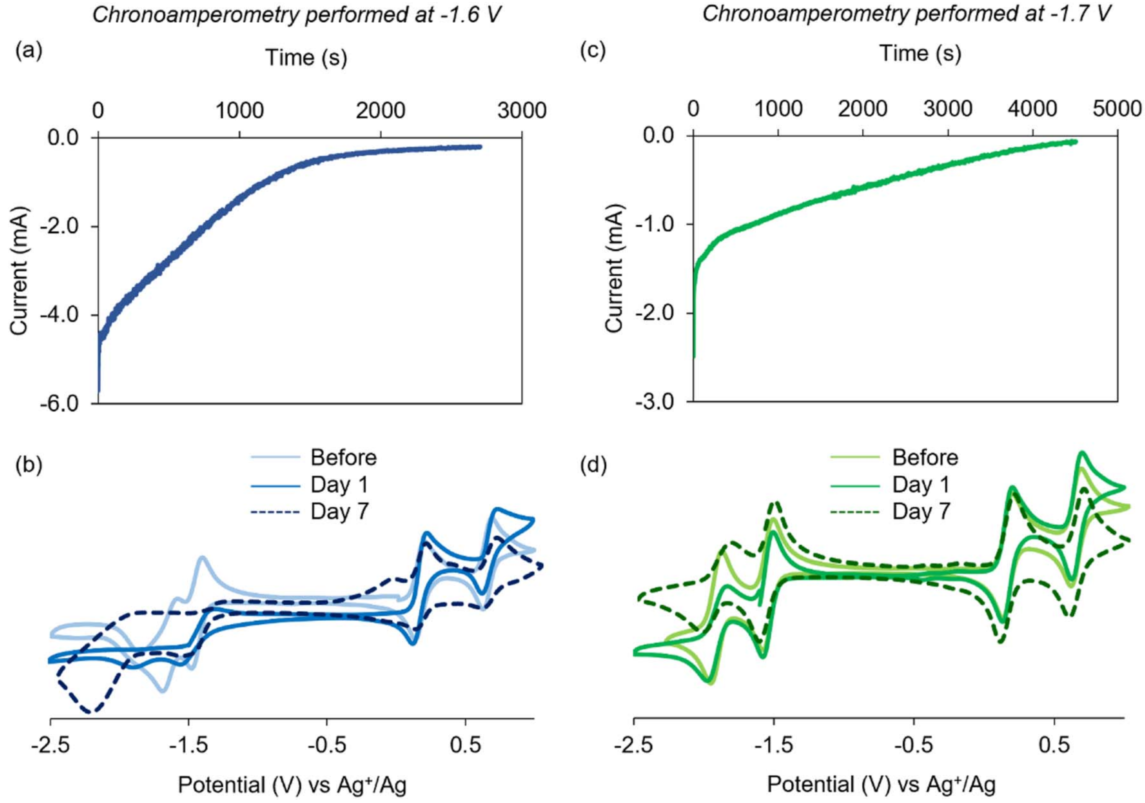

Fig. 6 Bulk reduction of $[Ti_2V_4O_5(OCH_3)_{14}]$ in acetonitrile with $LiPF_6$ (blue) and KPF_6 (green). (a and c) Represent the corresponding chronoamperometry curves. (b and d) Denote the CVs collected before and after bulk electrolysis.

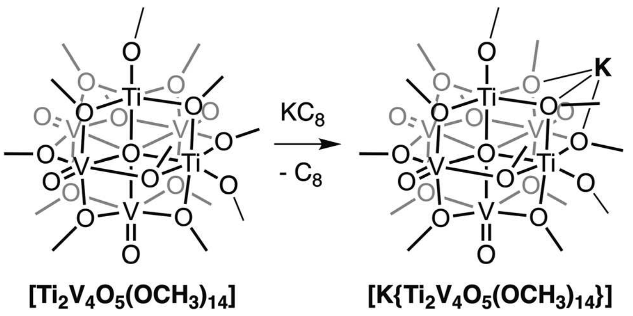

Scheme 2 Synthesis of $[K\{Ti_2V_4O_5(OCH_3)_{14}\}]$.

those reported for the molecular structure $[Ti_2V_4O_5(OMe)_{14}]$.[32] The maximum structural discrepancy was observed in the Ti–O_b (O_b = O atom of bridging alkoxide ligands) bond distances of the neutral species *versus* the potassium-bound assembly. Specifically, the Ti–O_b bonds are elongated in comparison to that of the neutral cluster, due to the sharing of electron density of the bridging oxygen atoms with the K^+ ion.

Structural analysis further provides additional insight into oxidation state distribution of transition metal ions composing the reduced TiPOV–alkoxide cluster. Oxidation states of titanium and vanadium were determined through bond valence sum calculations, using M–L bond distances from the X-ray structure data set obtained at 100 K. The bond valence parameters for V^{IV}, V^{V}, Ti^{III}, and Ti^{IV} along with the value of the universal constant *b* were taken from those reported by Brese and O'Keeffe.[42] The results are listed in Table S6.† All vanadium centers within the assembly were identified as tetravalent ions, resulting in an overall oxidation state distribution of V^{IV}_4. On the other hand, the Ti^{III}/Ti^{IV} ratio in the assembly was found to be

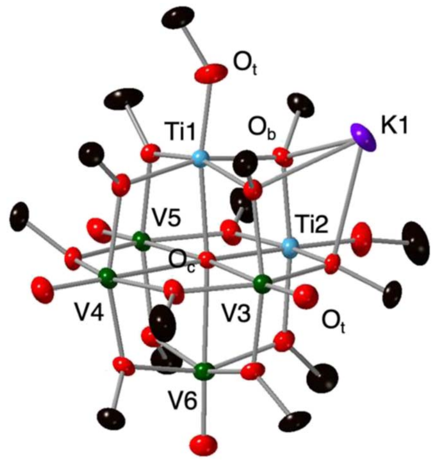

Fig. 7 Molecular structure of $[K\{Ti_2V_4O_5(OCH_3)_{14}\}]$ shown with 50% probability ellipsoids. Hydrogen atoms and solvent molecules have been removed for clarity. Key: black ellipsoids, C; red ellipsoids, O; light blue ellipsoids, Ti; dark green ellipsoids, V; purple ellipsoid, K.

This journal is © The Royal Society of Chemistry 2024

Published on 05 December 2023. Downloaded by University of Rochester on 2/27/2024 7:35:54 PM.

Table 1 Structural parameters of [K{$Ti_2V_4O_5(OCH_3)_{14}$}] and [$Ti_2V_4O_5(OMe)_{14}$] (O_b = O atom of bridging alkoxide ligands, O_t = terminal oxo ligand of vanadyl moieties, O_c = O atom positioned at the center of the cluster, V_c = *cis* vanadium centers, V_t = *trans* vanadium centers)

Bond	[K{$Ti_2V_4O_5(OCH_3)_{14}$}]	[$Ti_2V_4O_5(OMe)_{14}$]
Ti–O_b (avg)	2.018(3) Å	1.976 Å
Ti–O_c (avg)	2.146(3) Å	2.126 Å
Ti–O_t (avg)	1.814(3) Å	1.742 Å
K–O_b (avg)	2.741 Å	—
V=O_t (avg)	1.599(3) Å	1.601 Å
V_c–O_c	2.445(3) Å	2.373 Å
V_t–O_c	2.372(3) Å	2.473 Å

1 : 1 indicating the presence of an unpaired electron on one of the Ti centers. These observations confirm the formation of the mono-reduced species and the presence of localization of the reducing equivalent on titanium.

It should be noted that the atomistic insights are procured from the solid-state structure of [K{$Ti_2V_4O_5(OCH_3)_{14}$}], thus relevance of this model to the solution behavior of the reduced assembly must be taken with a grain of salt. Given our prior solution-phase results indicating significant evidence of ion-pairing interactions between the TiPOV and potassium ions, we anticipate that some degree of these interactions are relevant in MeCN. Binding of the potassium ion to the face of the cluster containing titanium centers suggests that interactions of the alkali ion with the reduced assembly impart additional stability to the cluster *via* the formation of formal bonding interactions to the surface of the TiPOV–alkoxide.

Impact of ion-pairing interactions on battery cycling

To further evaluate the influence of ion-pairing interactions between K^+ ions and $[Ti_2V_4O_5(OMe)_{14}]^{1-}$ on the stability of the cluster, we investigated the battery cycling characteristics through static charge–discharge experiments (Fig. 8). Our hypothesis is that the enhanced stability of the cluster will result in less decomposition of the charge carrier that will ultimately aid in improved battery performance. Thus, we performed galvanostatic cycling with potential holds (*vide supra*) in $TBAPF_6$ and KPF_6. Fig. 8a and b depict the charge–discharge trace of cycles 2 and 10 in $TBAPF_6$ and KPF_6, respectively (see full cycling data in Fig. S8†). Post cycling analysis by CV (Fig. 8c and d) demonstrates the stability of the positive electrolyte in the presence of both supporting electrolytes. In contrast, significant decomposition of the negative electrolyte is observed when $TBAPF_6$ is the supporting salt. Interestingly, we do not observe degradation of the negolyte in KPF_6 over 10 cycles. This result suggests that the stability of the reduced form of the cluster is improved in the presence of K^+ ions.

RFBs dissipate energy in the form of heat when consuming electric power in their working state.[43] This intrinsic attribute can produce activation, ohmic, and concentration losses during battery cycling as the reaction kinetics and transport properties of the electrolyte are functions of temperature.[44,45] These losses can result in the degradation of the active material that can further affect the battery performance metrics. The new redox feature emerging in the voltammogram of the negolyte after cycling (Fig. 8c) corresponds to the formation of the mono-titanium derivative of the TiPOV–alkoxide cluster, $[TiV_5O_6(OCH_3)_{13}]^{1-}$. The reversible peak at $\sim E_{1/2} = -0.18$ V in $TBAPF_6$ is a signature of the mono-titanium species. We note that the synthetic conditions prescribed for the formation of $[TiV_5O_6(OCH_3)_{13}]^{1-}$ require additional reductant, suggesting that formation of the mono-titanium derivative of the cluster is favored over the neutral [$Ti_2V_4O_5(OMe)_{14}$] complex under reducing conditions.[32]

To further prove that the observed decomposition is a combined result of reducing conditions and heat generation during battery operation, we heated the bulk reduced sample of [$Ti_2V_4O_5(OMe)_{14}$] at 30 °C and stirred it for 7 days to simulate the speculated heat generation during battery cycling (Fig. S9†). We observe that the solutions of [$Ti_2V_4O_5(OMe)_{14}$] in the presence of 0.1 M $TBAPF_6$ undergo significant degradation of the cluster, similar to those observed in postmortem analysis of charge–discharge cycling experiments. As such, the capacity of the system should decrease over time due to active material degradation. However, the overall normalized capacity decay in the case of $TBAPF_6$ is similar to that observed for KPF_6, albeit with lower absolute capacity values (Fig. 8e). Moreover, coulombic efficiencies were maintained at ≥90% over 10, indicative of quantitative electron transfer to and from the cluster (Fig. 8f). This indicates that the battery performance is not greatly affected by the observed decomposition. It should be noted that $[TiV_5(OCH_3)_{13}]^{1-}$ has been previously established as an energy-dense charge carrier by our team that operates within the employed potential window.[27] Consequently, the capacity will not decrease by large amounts as the cycling is still carried out by the mono-titanium species over a potential range that encloses the first reductive event of this redox couple (R1). Thus, while we see a drop in capacity over the first couple of cycles, it is stabilized henceforth at a lower capacity in the negative electrolyte as the generated species is stable and reversible.

In contrast, we observe minimal capacity fade (Fig. 8e) with KPF_6 yielding greater capacity per cycle under the same cycling conditions. To evaluate whether substituting the supporting electrolyte from $TBAPF_6$ to KPF_6 can maintain the stability of the charge carrier during long-term charge–discharge periods, we performed similar bulk reduction experiments in KPF_6 and evaluated the stability at 30 °C for 7 days. Our results demonstrate stability of the negolyte after 7 days (Fig. S10 and S11†) generated *via* bulk electrolysis with KPF_6 as the supporting electrolyte. We ascribe this behavior to the improved stability of the reduced cluster with KPF_6 as the supporting electrolyte.

Another reason for the undesirable degradation of the negative electrolyte in $TBAPF_6$ rather than KPF_6 can be attributed to the higher overpotentials required to meet the charge–discharge conditions in NAqRFBs. These overpotentials can lead to over-oxidation or over-reduction of the cluster to the doubly charged state, which may contribute to the instability of the system. Given that the observed decomposition germinates in reducing conditions, we propose that over-reduction of the cluster is another degradation pathway for the reported capacity

Published on 05 December 2023. Downloaded by University of Rochester on 2/27/2024 7:35:54 PM.

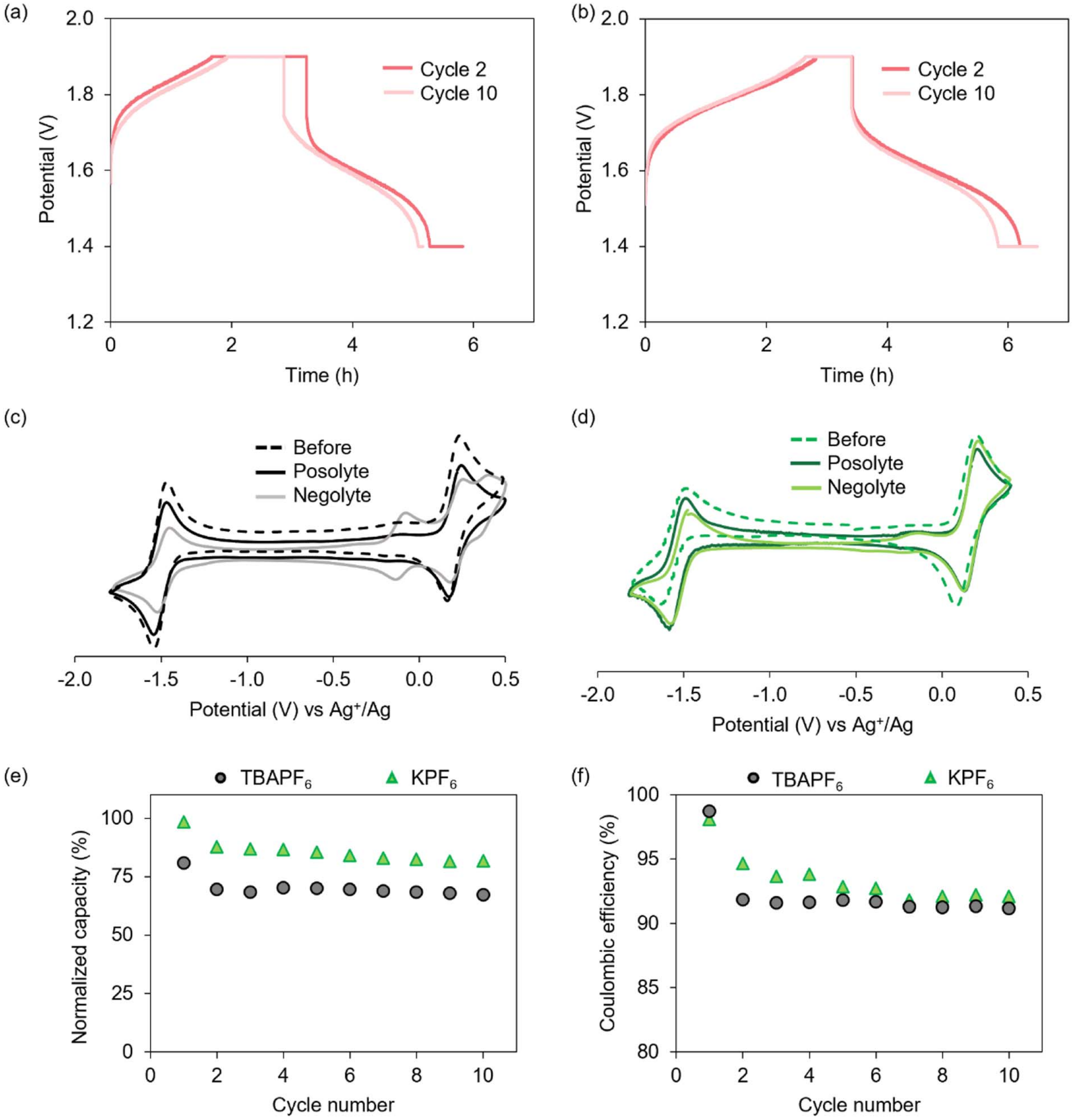

Fig. 8 Comparison of cycles 2 and 10 from the battery cycling experiment of $[Ti_2V_4O_5(OMe)_{14}]$ in (a) $TBAPF_6$ and (b) KPF_6. (c and d) Represent the corresponding CVs of the cluster after 10 charge–discharge cycles in $TBAPF_6$ and KPF_6, respectively. (e) Observed capacity normalized to theoretical capacity of 5 mM active species. (f) Coulombic efficiency over 10 cycles for both supporting electrolytes. The drop in coulombic efficiency from cycle 1 to 2 in both supporting electrolytes (C/D traces in (e) and (d)) is due to battery equilibration.

fade. To further attest this hypothesis, we performed bulk reduction of the cluster to −2 charge state in KPF_6 and monitored the obtained solution for 6 days (Fig. S19†). We have previously reported the instability of doubly reduced $[Ti_2V_4O_5(OMe)_{14}]$ in $TBAPF_6$.[27] Surprisingly, we do not observe any degradation of the di-reduced cluster in KPF_6 (Fig. S19b†). Moreover, the electrolyte system exhibits stability over one week as monitored *via* CV (Fig. S19c†). This experimental evidence suggests that we cannot rule out the possibility of over-reduction of the cluster under the employed cycling conditions and this degradation pathway is also likely responsible for exacerbating the battery performance in $TBAPF_6$.

The charge–discharge traces exhibit a single plateau in both cycling traces, indicative of a one electron transfer event (Fig. 8a and b). No additional plateaus are detected after 10 (dis)charge cycles in both supporting salts. Despite the same experimental conditions, the cluster reaches the potential limit earlier during the charge cycle in $TBAPF_6$. This behavior drives the programmatic transition to potentiostatic charging earlier as compared to KPF_6. A plausible reason can be sluggish electron transfer

Published on 05 December 2023. Downloaded by University of Rochester on 2/27/2024 7:35:54 PM.

kinetics that prolong the amount of time that the electrolyte spends in galvanostatic mode to reach the potential cutoff. To experimentally prove this hypothesis, we performed scan rate dependent CV measurements to first measure the diffusivity of the charge carriers. The obtained diffusion coefficients were then used to extract the rate constants of electron transfer by using Nicholson's method.

To determine the diffusion coefficients for $[Ti_2V_4O_5(OMe)_{14}]$, the redox events associated with O1 ($1^+/0$) and R1 ($0/1^-$) were isolated and CVs were recorded at scan rates ranging from 10–10 000 mV s^{-1} (Fig. 9 and S12–S14†). The plot of the peak current (i_p) *versus* the square root of scan rate ($\nu^{1/2}$) exhibits a linear dependence. This behavior is characteristic of a diffusion-limited electrochemical process, allowing for the assessment of the D_0 of $[Ti_2V_4O_5(OMe)_{14}]$ using the Randles–Sevcik (R–S) equation.[46,47] The calculated diffusion coefficients for O1 and R1 in 0.1 M KPF_6 are $5.15 \pm 0.27 \times 10^{-6}$ cm^2 s^{-1} and $1.06 \pm 0.07 \times 10^{-6}$ cm^2 s^{-1}, respectively. These values are similar to those reported previously for molecular RFB charge carriers in non-aqueous systems.[48,49]

As indicated in Fig. 9a, the diffusivity of $[Ti_2V_4O_5(OMe)_{14}]$ in acetonitrile for both redox couples (O1 and R1) is faster in the presence of $TBAPF_6$ as the supporting electrolyte (in comparison to KPF_6). We performed analysis on the reverse waves to retrieve the corresponding diffusion coefficients associated with the charged forms of the cluster *i.e.*, O1 and R1. In the case of reduction of $[Ti_2V_4O_5(OMe)_{14}]$, reduced diffusivity of the negatively charged species (R1 redox event) can be attributed to the differing charge compensation interactions arising from the non-specific binding of alkyl ammonium in contrast to the specific binding of potassium to the anionic TiPOV–alkoxide. The varied electrostatic interactions render the potassium atom tethered to the cluster as a contact-ion pair, which increases the molecular radius of the ensemble as compared to the neutral species. These ionic pairing interactions between the negatively charged cluster and K^+ ions necessitate that the ensemble is diffusing in the solution as a single entity. Thus, according to the Stokes–Einstein relationship, the diffusivity of the molecular species decreases with increased size. This explains the observed difference in diffusion coefficients of oxidized (O1) and reduced forms (R1) of $[Ti_2V_4O_5(OMe)_{14}]$ in 0.1 M KPF_6 solution.

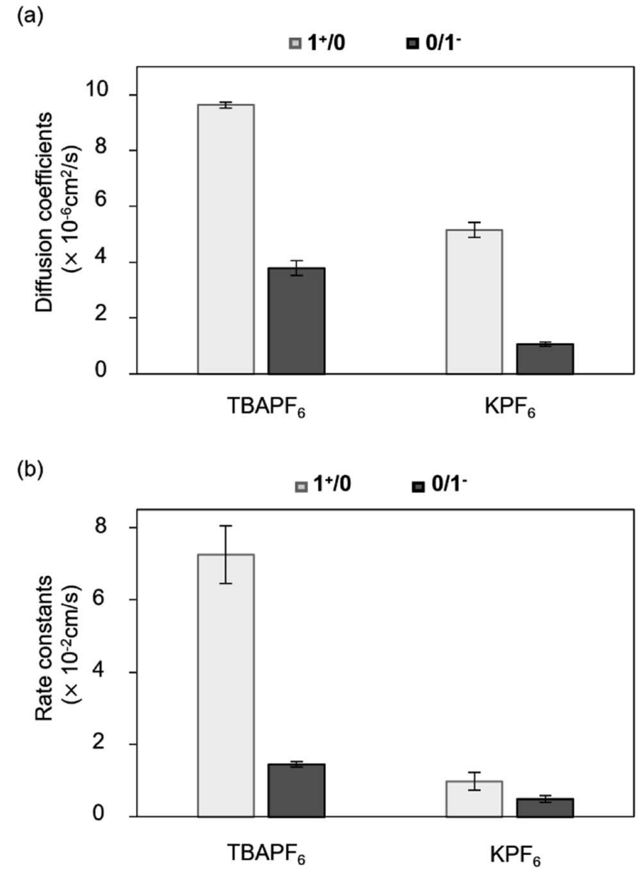

Fig. 9 Comparison of (a) diffusivity (b) heterogeneous rate constants of electron transfer for the redox events associated with O1 ($1^+/0$) and R1 ($0/1^-$) of $[Ti_2V_4O_5(OMe)_{14}]$ in $TBAPF_6$ and KPF_6.

Given the fact that there are little variations in the oxidative redox events between electrolyte systems, we were surprised to see a significant alleviation in the diffusion coefficients of the oxidized species in KPF_6. In considering the rationale behind these results, we evaluated the ionic mobility of the cationic species. The room temperature ionic mobility of K^+ is faster than TBA^+.[50] As such, K^+ ions have a greater tendency to migrate to the negatively charged electrode and accumulate at the electrode–electrolyte interface. Indeed, the role of alkali cations in affecting the charge distribution and electric field of the electrochemical double layer is well-established in the literature.[51–53] This phenomenon decreases the ability of the cluster to get oxidized at the electrode surface, which yields a smaller current response. Pilon and co-workers have illustrated the effect of concentration of species in the double layer on the ion diffusion coefficients as measured by cyclic voltammetry using a modified Poisson–Nernst–Planck relationship.[54] As the observed current is proportional to diffusivity in R–S analysis, we observe a smaller diffusion coefficient of the O1 redox couple in the case of KPF_6 as compared to $TBAPF_6$.

We next evaluated the heterogeneous rates of electron transfer in KPF_6 from the CV data using the Nicholson method (Fig. S15 and S16†).[55] The calculated values of k_0 for $1^+/0$ and $0/1^-$ of $[Ti_2V_4O_5(OMe)_{14}]$ in acetonitrile are plotted in Fig. 9b. As compared to our previously reported values in 0.1 M $TBAPF_6$ (O1 $= 7.2 \pm 0.08 \times 10^{-2}$ cm s^{-1}; R1 $= 1.4 \pm 0.01 \times 10^{-2}$ cm s^{-1}),[31] the rate constants of electron transfer are approximately an order of magnitude slower in KPF_6 (O1 $= 9.7 \pm 0.25 \times 10^{-3}$ cm s^{-1}; R1 $= 4.9 \pm 0.09 \times 10^{-3}$ cm s^{-1}). We attribute this behavior to the enhanced conduction of the redox active species that can increase the effective rate of charge transfer. Indeed, impedance values recorded at 100 kHz prior to CV measurements reveal a smaller R_Ω for $TBAPF_6$, which enhances its propensity to exhibit faster heterogeneous kinetics. Thus, these observations collectively explain the distinct shapes of the (dis)charge curves in both electrolytes.

Overall, these results provide a significant first step in realizing alternate supporting electrolytes for stable cycling over extended periods of time. In addition, the supporting salt

Published on 05 December 2023. Downloaded by University of Rochester on 2/27/2024 7:35:54 PM.

contributes to the total molecular weight by providing counter ions to the charged species formed during battery cycling. Thus, employing supporting electrolytes with low equivalent weights significantly reduces the overall molecular weight of the charged species formed during oxidation and reduction of the battery analyte. This ultimately helps in improving the gravimetric energy density of the battery. Moreover, pivoting away from tetrabutylammonium based electrolytes can aid in reducing the cost associated with the electrolyte system.

Conclusions

In this study, we describe the impact of supporting electrolyte on the stability of TiPOV–alkoxide cluster, $[Ti_2V_4O_5(OMe)_{14}]$. Cyclic voltammetry studies reveal a shift in the electrochemical potentials of the reduction events towards positive values in KPF_6, indicating stability of the cluster. Substoichiometric titrations with alkali cations (Li^+ and K^+) in different supporting electrolytes demonstrate the influence of the identity of the charge compensating cation on the electrochemical reversibility of the cluster's reduction events. We illustrate that the decomposition of the reduced species, which is one of the bottlenecks in the success of these charge carriers, is cation dependent with enhanced stability in weakly coordinating KPF_6 and decreased stability with harder Li-based coordinating electrolytes. Thus, we identify KPF_6 as a better supporting electrolyte than the ubiquitous $TBAPF_6$ as it prevents degradation of the negolyte during battery cycling. Moreover, developing charge carriers with lower molecular mass per mole of electron transferred are important future targets as they allow to increase the effective concentration of the active material thereby providing the high energy densities that are required for practical NAqRFB electrolytes. In this regard, the proposed supporting electrolyte provides distinct advantages over other alkali metal and tetraalkylammonium salts. Our results highlight that the supporting salts can function beyond their traditional roles by tuning the charge compensation energetics that are critical for improved battery chemistries. We anticipate that these results will motivate further avenues in the rational design of the overall electrolyte system.

Author contributions

MD and EMM conceived and planned the experiments. MD performed all synthetic and electrochemical experiments and interpreted results. WWB performed structural analysis of single crystals of $[K\{Ti_2V_4O_5(OCH_3)_{14}\}]$ provided by MD. All authors contributed in the writing of the manuscript.

Conflicts of interest

There are no conflicts to declare.

Acknowledgements

This research was funded by the National Science Foundation, Division of Chemical, Bioengineering, and Environmental, and Transport Systems Program (Award 2015749). EMM is a recipient of a Camille Dreyfus Teacher Scholar Award from the Camille and Henry Dreyfus Foundation that has also financially supported this research.

References

1 Z. G. Yang, J. L. Zhang, M. C. W. Kintner-Meyer, X. C. Lu, D. W. Choi, J. P. Lemmon and J. Liu, *Chem. Rev.*, 2011, **111**, 3577–3613.
2 B. Dunn, H. Kamath and J. M. Tarascon, *Science*, 2011, **334**, 928–935.
3 G. L. Soloveichik, *Chem. Rev.*, 2015, **115**, 11533–11558.
4 K. Gong, Q. R. Fang, S. Gu, S. F. Y. Li and Y. S. Yan, *Energy Environ. Sci.*, 2015, **8**, 3515–3530.
5 M. Park, J. Ryu, W. Wang and J. Cho, *Nat. Rev. Mater.*, 2017, **2**, 16080–16098.
6 R. M. Darling, K. G. Gallagher, J. A. Kowalski, S. Ha and F. R. Brushett, *Energy Environ. Sci.*, 2014, **7**, 3459–3477.
7 R. Dmello, J. D. Milshtein, F. R. Brushett and K. C. Smith, *J. Power Sources*, 2016, **330**, 261–272.
8 L. Y. Zhang, R. Z. Feng, W. Wang and G. H. Yip, *Nat. Rev. Chem*, 2022, **6**, 524–543.
9 M. J. Hazelrigg and A. J. Bard, *J. Electrochem. Soc.*, 1975, **122**, 211–220.
10 B. G. Chauhan, W. R. Fawcett and A. Lasia, *J. Phys. Chem.*, 1977, **81**, 1476–1481.
11 K. Hernandez-Burgos, G. G. Rodriguez-Calero, W. D. Zhou, S. E. Burkhardt and H. D. Abruna, *J. Am. Chem. Soc.*, 2013, **135**, 14532–14535.
12 C. R. DeBlase, K. Hernandez-Burgos, J. M. Rotter, D. J. Fortman, D. D. Abreu, R. A. Timm, I. C. N. Diogenes, L. T. Kubota, H. D. Abruna and W. R. Dichtel, *Angew. Chem., Int. Ed.*, 2015, **54**, 13225–13229.
13 K. H. Hendriks, C. S. Sevov, M. E. Cook and M. S. Sanford, *ACS Energy Lett.*, 2017, **2**, 2430–2435.
14 X. L. Wei, W. Xu, J. H. Huang, L. Zhang, E. Walter, C. Lawrence, M. Vijayakumar, W. A. Henderson, T. B. Liu, L. Cosimbescu, B. Li, V. Sprenkle and W. Wang, *Angew. Chem., Int. Ed.*, 2015, **54**, 8684–8687.
15 F. F. Zhong, M. H. Yang, M. Ding and C. K. Jia, *Front. Chem.*, 2020, **8**, 451.
16 N. H. Mitchell and N. Elgrishi, *J. Phys. Chem. C*, 2023, **127**, 10938–10946.
17 J. L. Barton, A. I. Wixtrom, J. A. Kowalski, E. A. Qian, D. Jung, F. R. Brushett and A. M. Spokoyny, *ACS Appl. Energy Mater.*, 2019, **2**, 4907–4913.
18 M. Milton, Q. Cheng, Y. Yang, C. Nuckolls, R. H. Sanchez and T. J. Sisto, *Nano Lett.*, 2017, **17**, 7859–7863.
19 C. L. Peake, A. J. Kibler, G. N. Newton and D. A. Walsh, *ACS Appl. Energy Mater.*, 2021, **4**, 8765–8773.
20 C. Modrzynski and P. Burger, *Dalton Trans.*, 2019, **48**, 1941–1946.
21 M. B. Freeman, L. Wang, D. S. Jones and C. M. Bejger, *J. Mater. Chem. A*, 2018, **6**, 21927–21932.
22 L. E. Vangelder, A. M. Kosswattaarachchi, P. L. Forrestel, T. R. Cook and E. M. Matson, *Chem. Sci.*, 2018, **9**, 1692–1699.

This journal is © The Royal Society of Chemistry 2024

Published on 05 December 2023. Downloaded by University of Rochester on 2/27/2024 7:35:54 PM.

23 L. E. VanGelder, B. E. Petel, O. Nachtigall, G. Martinez, W. W. Brennessel and E. M. Matson, *Chemsuschem*, 2018, **11**, 4139–4149.

24 B. E. Schurr, O. Nachtigall, L. E. VanGelder, J. Drappeau, W. W. Brennessel and E. M. Matson, *J. Coord. Chem.*, 2019, **72**, 1267–1286.

25 L. E. VanGelder, E. Schreiber and E. M. Matson, *J. Mater. Chem. A*, 2019, **7**, 4893–4902.

26 L. E. VanGelder, W. W. Brennessel and E. M. Matson, *Dalton Trans.*, 2018, **47**, 3698–3704.

27 L. E. Vangelder and E. M. Matson, *J. Mater. Chem. A*, 2018, **6**, 13874–13882.

28 S. Himeno, M. Takamoto and T. Ueda, *J. Electroanal. Chem.*, 2000, **485**, 49–54.

29 J. M. Gómez-Gil, E. Laborda, J. Gonzalez, A. Molina and R. G. Compton, *J. Phys. Chem. C*, 2017, **121**, 26751–26763.

30 E. Schreiber, N. A. Hartley, W. W. Brennessel, T. R. Cook, J. R. McKone and E. M. Matson, *ACS Appl. Energy Mater.*, 2019, **2**, 8985–8993.

31 M. Dagar, M. Corr, T. R. Cook, J. R. McKone and E. M. Matson, *J. Mater. Chem. A*, 2023, **11**, 13729–13741.

32 L. E. Vangelder, P. L. Forrestel, W. W. Brennessel and E. M. Matson, *Chem. Commun.*, 2018, **54**, 6839–6842.

33 G. R. Fulmer, A. J. M. Miller, N. H. Sherden, H. E. Gottlieb, A. Nudelman, B. M. Stoltz, J. E. Bercaw and K. I. Goldberg, *Organometallics*, 2010, **29**, 2176–2179.

34 G. Sheldrick, *Acta Crystallogr., Sect. C: Struct. Chem.*, 2015, **71**, 3–8.

35 J. C. Myland and K. B. Oldham, *Anal. Chem.*, 2000, **72**, 3972–3980.

36 M. A. Goulet and M. J. Aziz, *J. Electrochem. Soc.*, 2018, **165**, A1466–A1477.

37 S. E. Group and R. Greef, *Instrumental Methods in Electrochemistry*, Ellis Horwood, 1990.

38 T. Kawamura, S. Okada and J.-i. Yamaki, *J. Power Sources*, 2006, **156**, 547–554.

39 C. L. Campion, W. T. Li and B. L. Lucht, *J. Electrochem. Soc.*, 2005, **152**, A2327–A2334.

40 W. A. L. Izonfuo and E. R. Malinowski, *Indian J. Chem., Sect. A: Inorg., Bio-inorg., Phys., Theor. Anal. Chem.*, 1989, **28**, 361–365.

41 C. Daniel and H. Hartl, *J. Am. Chem. Soc.*, 2009, **131**, 5101–5114.

42 N. E. Brese and M. Okeeffe, *Acta Crystallogr., Sect. B: Struct. Sci.*, 1991, **47**, 192–197.

43 S. L. Huang, C. P. Li, C. C. Chang, C. C. Tseng, M. W. Wang and M. L. Chen, *Energies*, 2020, **13**, 6717–6736.

44 D. E. Eapen, S. R. Choudhury and R. Rengaswamy, *Appl. Surf. Sci.*, 2019, **474**, 262–268.

45 J. Y. Ren, Y. J. Li, Z. Y. Wang, J. Sun, Q. L. Yue, X. Z. Fan and T. S. Zhao, *Int. J. Heat Mass Transfer*, 2023, **203**, 123818–123838.

46 Q. H. Liu, A. E. S. Sleightholme, A. A. Shinkle, Y. D. Li and L. T. Thompson, *Electrochem. Commun.*, 2009, **11**, 2312–2315.

47 A. A. Shinkle, A. E. S. Sleightholme, L. T. Thompson and C. W. Monroe, *J. Appl. Electrochem.*, 2011, **41**, 1191–1199.

48 Y. Ding, Y. Zhao, Y. T. Li, J. B. Goodenough and G. H. Yu, *Energy Environ. Sci.*, 2017, **10**, 491–497.

49 F. Pan and Q. Wang, *Molecules*, 2015, **20**, 20499–20517.

50 P. H. Barry and J. W. Lynch, *J. Membr. Biol.*, 1991, **121**, 101–117.

51 P. Sebastian-Pascual, Y. Shao-Horn and M. Escudero-Escribano, *Curr. Opin. Electrochem.*, 2022, **32**, 100918.

52 G. Leverick and Y. Shao-Horn, *Adv. Energy Mater.*, 2023, **13**, 2204094.

53 B. Huang, K. H. Myint, Y. Wang, Y. Zhang, R. R. Rao, J. Sun, S. Muy, Y. Katayama, J. Corchado Garcia, D. Fraggedakis, J. C. Grossman, M. Z. Bazant, K. Xu, A. P. Willard and Y. Shao-Horn, *J. Phys. Chem. C*, 2021, **125**, 4397–4411.

54 H. N. Wang, A. Thiele and L. Pilon, *J. Phys. Chem. C*, 2013, **117**, 18286–18297.

55 R. S. Nicholson, *Anal. Chem.*, 1965, **37**, 1351–1355.